De-coupling of optical and electrical properties in front TCO using the bilayer concept for thin-film solar cells

Saitta, Federica; Kalpoe, Prashand; Ahluwalia, Vidur; Padmakumar, Govind; Rodriguez, Paula Perez; Limodio, Gianluca; Santbergen, Rudi; Smets, Arno H.M.

DOI
10.1016/j.solmat.2025.113723

Publication date
2025

Document Version
Final published version

Published in
Solar Energy Materials and Solar Cells

Citation (APA)
Saitta, F., Kalpoe, P., Ahluwalia, V., Padmakumar, G., Rodriguez, P. P., Limodio, G., Santbergen, R., & Smets, A. H. M. (2025). De-coupling of optical and electrical properties in front TCO using the bilayer concept for thin-film solar cells. *Solar Energy Materials and Solar Cells*, *290*, Article 113723. https://doi.org/10.1016/j.solmat.2025.113723

Solar Energy Materials & Solar Cells 290 (2025) 113723

Contents lists available at ScienceDirect

Solar Energy Materials and Solar Cells

journal homepage: www.elsevier.com/locate/solmat

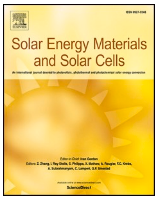

De-coupling of optical and electrical properties in front TCO using the bilayer concept for thin-film solar cells

Federica Saitta *, Prashand Kalpoe, Vidur Ahluwalia, Govind Padmakumar, Paula Perez Rodriguez, Gianluca Limodio, Rudi Santbergen, Arno H.M. Smets

Photovoltaic Materials and Devices (PVMD) Group, Delft University of Technology, Mekelweg 4, Delft, the Netherlands

ABSTRACT

This study investigates the transparent conductive oxides (TCOs) as front contact for thin-film solar cell applications by developing a bilayer design that decouples the optical and electrical functionalities. The bilayer front contact structure combines hydrogenated indium oxide (IOH) and non-intentionally doped zinc oxide (ZnO) materials. This design achieves enhanced optoelectrical properties with a mobility of 120 cm^2/Vs and a carrier density of $1.97\cdot10^{19}$ cm^{-3}. Notably, the bilayer outperforms the expected average of its constituent layers in both transparency and conductivity, reflecting the benefits of optimized layer architecture. When integrated as the front electrode in a hydrogenated nanocrystalline silicon (nc-Si:H) solar cell, the IOH/ZnO bilayer yields a fill factor of 64.56 % and a power conversion efficiency of 7.85 %. When using an ITO front contact, the nc-Si:H solar cell reveals a fill factor of 56.27 % and an efficiency of 6.80 %. By successfully decoupling optical and electrical properties, the optimized IOH/ZnO bilayer offers a significant advancement over single-layer TCO configurations, presenting an innovative pathway for enhanced performance in thin-film solar cell technology.

1. Introduction

Transparent conductive oxide (TCO) materials are commonly employed as front contact electrode for any thin-film (TF) solar cell [1,2]. Numerous materials have been employed as TCOs, and among these options, metal oxides attract attention as a preferable choice for achieving superior optoelectrical characteristics [3–6]. The optical and electrical properties of metal oxides rely upon the oxidation state of the metal constituent and, the nature and quantity of impurities integrated in the films [7–9].

In_2O_3-based TCOs, such as indium tin oxide (ITO), are widely used as front electrodes in solar cells due to their trade-off between high electrical conductivity and good transparency in the visible light spectrum [10,11]. However, the simultaneous optimization of both transparency and conductivity in a single TCO layer is always limited by a compromise solution [12]. Higher carrier concentration improves conductivity but reduces transparency in the near infrared (NIR) region due to free carrier absorption (FCA) [8,13].

The concept of using bilayer TCO structures to overcome the inherent compromise between transparency and conductivity in a single-layer TCOs has been explored in previous studies [14]. For instance, Lee et al. demonstrated that a double-layer transparent conductive oxide structure composed of ITO and niobium-doped titanium dioxide (TNO) effectively serves as an anti-reflection coating, significantly reducing front surface reflectance and ensuring adequate lateral conductivity in silicon solar cells [15].

Additionally, indium tin oxide/aluminum-doped zinc oxide (AZO) bilayer TCO films have emerged as a highly effective front electrode architecture for thin-film silicon solar cells. Studies have demonstrated that these bilayers exhibit superior structural and morphological properties, along with enhanced optoelectrical characteristics, surpassing those of single-layer TCO films [16–18].

Similarly, Tan et al. revealed that a bilayer of hydrogenated indium oxide (IOH) and low-pressure chemical vapor deposition (LPCVD) ZnO in modulated surface textured (MST) electrodes significantly enhances the performance of multijunction TF silicon solar cells. This bilayer effectively minimizes parasitic absorption and ensures efficient light management, leading to higher initial and stabilized efficiencies of solar cells compared to single-layer TCOs [19].

Previous studies primarily focused on material selection and performance metrics of TCOs used as front contacts. However, the underlying mechanisms that enable the decoupling of optical and electrical functionalities in bilayer TCO structures remain insufficiently understood. The novelty of this work lies in its fundamental analysis of the free charge carrier transport mechanisms governing bilayer TCO behavior, offering a deeper understanding of their enhanced optoelectrical properties.

The investigation is therefore directed towards the designing and

---

* Corresponding author.
E-mail address: f.s.saitta@tudelft.nl (F. Saitta).

https://doi.org/10.1016/j.solmat.2025.113723
Received 24 December 2024; Received in revised form 27 March 2025; Accepted 12 May 2025

optimization of a two film-stack front contact for TF solar cells, employing the sputtering technique as the fabrication method. In addition to its compatibility with high-quality TCO deposition, sputtering is a relatively low-cost and scalable process, making it attractive for industrial applications [1]. In this bilayer design, one TCO is chosen primarily for its high transparency, while the second selected TCO is intended to provide high conductivity (Section 3.1). Various TCO metal oxides are analyzed to identify the most suitable candidates, considering the intricate interplay between their optical and electrical properties [20,21].

By refining the bilayer design (Section 3.4) and optimizing the properties of each TCO layer (Section 3.2 and 3.3), significant enhancements in both optical and electrical performance are achieved (Section 3.4.2). Based on the laws of multilayer optics and conductivity, one might expect the bilayer's overall transparency and conductivity to merely reflect the average of its constituent layers. However, the optimized design surpasses these expectations, delivering superior values in both metrics. While this study employs particular TCO materials, the understanding of the working principles behind the TCOs bilayer structure (Section 3.4.3) is broadly applicable. It not only facilitates significant improvements in the performance and efficiency of TF solar cells (Section 3.5) [19,22] but also offers the way for innovative front-contact designs in a broader range of solar cell technologies [23], potentially using more cost-effective TCO alternatives.

2. Experimental procedure

This section outlines the methodologies used for the fabrication, characterization, and evaluation of TCO films and solar cells. Section 2.1 details the deposition process of various TCO materials and the post-deposition annealing (PDA) treatment. Section 2.2 describes the optical, electrical, and structural characterization techniques employed to assess the properties of the fabricated TCOs. Section 2.3 and 2.4 discuss the key optical and electrical performance metrics relevant to front-contact applications in solar cells. Finally, Section 2.5 presents the fabrication and characterization of hydrogenated nanocrystalline silicon (nc-Si:H) solar cells incorporating the developed bilayer TCO front contact.

2.1. *TCO fabrication and post-deposition annealing (PDA) treatment*

The TCO films are grown on corning glass substrates by using Radio Frequency (RF, 13.56 MHz) magnetron sputtering technique. The geometrical size of the substrate is 10 cm x 2.5 cm x 0.7 mm. Prior to sputtering, each glass substrate is cleaned in acetone and isopropyl alcohol ultrasonic baths for 10 min respectively. Four different types of transparent conductive materials are subjected to investigation. They are hydrogen-doped indium oxide (IOH), tin-doped indium oxide (ITO), aluminum-doped zinc oxide (AZO) and non-intentionally doped zin oxide (ZnO).

These films were fabricated in a multi-chamber sputtering tool. Deposition time, power, and temperature are adjusted to investigate various sputtering conditions. In the case of IOH, the introduction of hydrogen is achieved by varying the partial pressure of water (H_2O) vapor. Table 2.1 presents the power density (P) and substrate temperature (T) window ranges for each investigated TCO.

Table 1
Range of power density [W/cm^2] and substrate temperature [°C] windows, varied as deposition parameters for the investigated TCOs.

material	P_{min} [W/cm^2]	P_{max} [W/cm^2]	T_{min} [°C]	T_{max} [°C]
ITO	1.35	3.00	25	156
IOH	1.05	1.80	25	107
ZnO	1.00	4.00	95	217
AZO	1.00	4.00	95	217

The deposited TCO samples are subjected to post-deposition annealing (PDA) treatment under controlled heating time and temperature. Annealing is performed both in ambient environment and in vacuum to achieve an optimal improvement in opto-electrical properties. The vacuum annealing is conducted with and without the H_2 gas flow.

2.2. *TCO characterization*

Optically, the transmittance (T) and reflectance (R) spectra are measured by spectrophotometric PerkinElmer Lambda 1050 system and, the absorbance (A) is derived by applying the law of energy conservation ($1 = A + R + T$) for light interaction with materials.

The spectroscopic ellipsometry (SE) M-2000DI system (J.A. Woollam Co., Inc.) is used to determine bulk thickness (t), refractive index (n), extinction coefficient (k) and optical bandgap (E_g) from Tauc plot according to SE-fitted absorption coefficient (α) curve. In SE analysis, the dielectric function of TCOs sample is considered homogenous in depth and modelled by combining two oscillator theories: Cody-Lorentz and Drude.

Furthermore, the TCOs thickness is also determined by a Steag ETA-Optik mini-RT setup. In mini-RT measurements, R and T curves are measured and processed through Scout software to estimate the sample thickness.

Electrically, the TCO is characterized by the resistivity (ρ), the sheet resistance (R_{sh}), the carrier density (N) and mobility (μ). The ρ is determined from HMS-5000 Hall Effect measurement system by using the so-called van der Pauw method, and then N and μ are derived combined with the Hall effect at room temperature. The magnetic flux density is set at 0.55 T, the input current at 10 mA and the sample thickness is tested in advance with mini-RT setup. The probes are arranged in a square configuration, approximately 1 cm apart, ensuring consistent spacing for accurate measurements. The R_{sh} is measured using the four-point probe (4 PP) method with the AIT CMT-SR2000N measurement system, where four equidistantly positioned contacts are linearly arranged.

In addition to the optoelectrical measurements, the material characterization is conducted on the TCO samples to gain a more comprehensive understanding of their properties.

The crystalline nature of the films is analyzed by using X-ray diffraction (XRD). The XRD spectra is obtained with Bruker D8 Advance diffractometer Bragg-Brentano geometry and, Cu Kα radiation (wavelength of 1.5406 Å) is employed from the X-ray tube with a standard focus. The morphological images of the samples are captured employing a Hitachi Regulus 8230 field-emission scanning electron microscope (SEM). The Bruker atomic force microscopy (AFM) setup is used for high-resolution imaging and studying of the surface topography. The image processing and the data analysis are performed with Gwydion software.

2.3. *Optical metrics*

In a solar cell, the TCO-based front contact contributes to parasitic absorption above the optical bandgap in the ultraviolet (UV) region, and in the near infrared (NIR) region of the solar spectrum due to the free carrier absorption (FCA).

A broader transparency window can be achieved through two primary approaches. Firstly, selecting a TCO material with a larger optical energy bandgap can extend the material's capability for optical transparency across a wider wavelength range in the UV region [24]. Secondly, an extended transparency window can also be attained through the Moss-Burstein shift, which occurs when a high carrier concentration fills the lower-energy states in the conduction band, effectively increasing the apparent bandgap of the TCO material [25].

In the NIR wavelength region (above 700 nm), the TCO optical absorption is influenced by intra-band transitions occurring within the conduction band [26]. The modelling of the FCA is often carried out using the Drude oscillator. According to this theory, the absorption coefficient (α_{FCA}) is calculated as [26,27]:

$$\alpha_{FCA} = \frac{\lambda^2\ e^3\ N_e}{4\ \pi^2\ \varepsilon_0\ c^3\ n\ (m_e{}^*)^2\ \mu_{opt}} \tag{2.1}$$

where λ is the wavelength of the incident light, e is the elementary charge, N_e is the electrons carrier concentration for n-type doped TCOs, ε_0 is the vacuum permittivity, c is the speed of light in vacuum, n is the TCO refractive index at one particular wavelength, $m_e{}^*$ is the effective electron mass and, μ_{opt} is the optical mobility.

As shown in Formula 2.1, the α_{FCA} is directly proportional to N_e and an increase of the carrier concentration enhances the probability of photon-carrier interaction [28]. This increase results in a greater FCA effect. In the case of TCO front contact, the minimization of N_e reduces unwanted absorption of the NIR light and ensures the material transparency in this specific spectral range.

2.4. Electrical metrics

A device-relevant parameter used for assessing the TCOs electrical properties is the sheet resistance (R_{sh}). The sheet resistance is a crucial metric that provides insights into the electrical conductivity (σ) and, it is calculated as [7]:

$$R_{sh} = \frac{1}{\sigma\ t} = \frac{1}{e\ N_e\ \mu\ t} \tag{2.2}$$

where t is the thickness of the TCO material and μ is the electron mobility when an n-type doped TCO film is considered.

For the optimization of the front contact, low R_{sh} is crucial to minimize electrical losses towards metal electrodes. The TCO conductivity can be enhanced either by increasing carrier density (N_e) or improving carrier mobility (μ). However, increasing carrier density through doping can lead to higher free carrier absorption (see equation (2.1)) and reduced relaxation times due to dopant scattering, impacting the material's optical and electrical performance. This shows that achieving optimal performance in a TCO front contact is a challenge due to the complex interplay between its electrical and optical characteristics. High carrier mobility and a moderate level of carrier concentration are essential for combining low sheet resistance with good transparency.

2.5. Solar cell fabrication

Hydrogenated nanocrystalline silicon (nc-Si:H) single-junction solar cells (4 x 4 mm^2) are fabricated to evaluate the performance effects of the developed bilayer front contact design, which decouples the optical and electrical properties. Three different front electrodes are sputtered on micro-textured glass substrates with morphology features in the order of 1–3 μm commonly used to achieve efficient light trapping in the state-of-the-art devices [29]. The front contacts include 150 nm of ITO, 150 nm of IOH as a monolayer, and a bilayer design with 150 nm of IOH and 1 μm of ZnO. The choice of a 150 nm thickness is particularly critical, as it ensures full coverage and prevents any part of the craters on the textured glass from being left uncovered.

Additionally, an intermediate ambient PDA treatment is applied to the front contact during the solar cells fabrication. The ITO or IOH monolayers are annealed for 20 min, while the IOH/ZnO bilayer for 2h and 20 min.

Superstrate-type *p-i-n* nc-Si:H solar cells are deposited using plasma-enhanced chemical vapor deposition (PECVD) and have a configuration consisting of 16 nm p-SiO$_x$:H/2.6 μm i-nc-Si:H/20 nm n-SiO$_x$:H. A 10 nm ZnO buffer layer is included between the front contact and the p-i-n structure. The metal back contact is thermally evaporated, comprising 300 nm Ag/30 nm Cr/800 nm Al. A schematic representation of the solar cell architecture is provided in Fig. 13 (Section 3.5) for reference.

The solar cells performance is evaluated by measuring current-voltage (JV) characteristics with an AM 1.5g solar simulator (100 mW/cm^2) at 25 °C. Open circuit voltage (V_{oc}), fill factor (FF), power conversion efficiency (η), series resistance (R_s) and shunt resistance (R_{sh}) are also recorded.

The external quantum efficiency (EQE) measurements are performed with monochromatic light setup, from which the short-circuit current density ($J_{sc,EQE}$) is determined. The total absorptance (1-R) is derived from the reflectance measured with the spectrophotometric system.

3. Results and discussion

This section focuses on the characterization of both single-layer and bilayer TCOs deposited on glass, with particular attention to their optical and electrical properties, as detailed in Sections 3.1 to 3.4.

The bilayer is constructed using two types of sputtered TCOs available in the lab: one with the highest lateral conductivity (IOH) and another with the highest optical transmittance in the NIR region (ZnO), as described in Section 3.1. The electrical and optical properties of the individual layers are optimized in Sections 3.2 and 3.3. Section 3.4 presents the processing and optimization of the IOH/ZnO bilayer. In Section 3.4.2, it is shown that the bilayer's charge carrier density and mobility outperform the simple superposition of the properties of the two single layers. Section 3.4.3 explains the physical mechanism underlying the decoupling of electrical and optical properties in the bilayer structure. Finally, Section 3.5 demonstrates the integration of the bilayer into a hydrogenated nanocrystalline silicon (nc-Si:H) solar cell and compares its performance to devices using single-layer TCOs.

3.1. TCO selection for bilayer

To identify the most suitable TCO candidates, one offering the highest lateral conductivity and the other the highest transmittance in the NIR region, a comparative analysis is conducted based on the absorption coefficient at 1100 nm and the resistivity. The wavelength of 1100 nm is used because it falls within the NIR range and is often used in various optical and photovoltaic research contexts to evaluate the performance of materials in the NIR spectrum.

In Fig. 1, the optoelectrical properties of each material exhibit scattered data points due to the changes made in deposition parameter

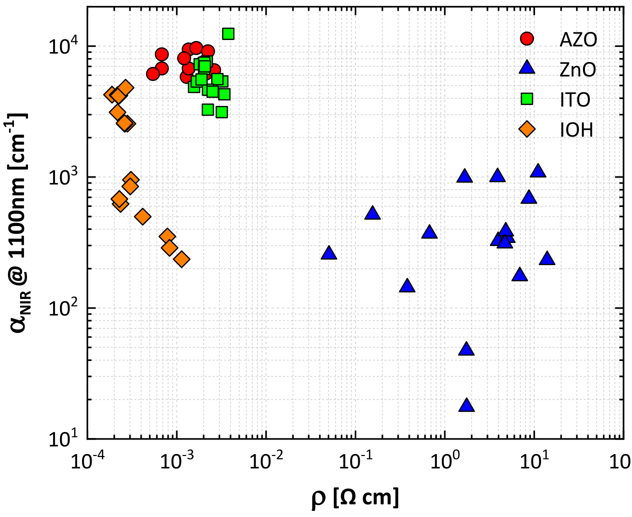

Fig. 1. Absorption coefficient [cm^{-1}] @ λ = 1100 nm vs resistivity [Ω cm] of processed TCOs: hydrogen-doped indium oxide (IOH), tin-doped indium oxide (ITO), aluminum-doped zinc oxide (AZO) and zin oxide (ZnO).

space.

Among the investigated TCOs, AZO and ITO are highly absorptive in the NIR region. The absorption coefficient values are all above $3.0\cdot10^{3}$ cm^{-1} in the NIR region, whereas the minimum resistivity reached is $5.0\cdot10^{-3}$ Ω cm. IOH samples reveal the lowest ρ values, ranging between $9.0\cdot10^{-3}$ and $7.0\cdot10^{-3}$ Ω cm. The IOH material shows a broader distribution of α_{NIR} values between $2.0\cdot10^{2}$ and $5.0\cdot10^{3}$ cm^{-1}. These findings align with previous studies on hydrogenated indium oxide films, which report comparable resistivity values and near-infrared absorption characteristics under similar sputtering conditions [30,31].

Despite the widely varying characteristics of ZnO, Fig. 1 underlines the poor conductivity of such undoped material and the highest transparency in the NIR region. The ZnO emerges as the most suitable TCO due to its low FCA losses, while IOH consistently achieves the highest conductivity values among all the examined TCOs. Hence, the undoped zinc oxide and the hydrogenated indium oxide materials are chosen for the bilayer design.

3.2. Hydrogenated indium oxide deposition parameters and PDA optimization

Once the IOH material is selected as the optimal choice for the first layer deposited in the bilayer structure, the deposition conditions are fine-tuned within a narrow power density range of 1.3–1.8 W/cm^{2}. The impact of ambient PDA on α_{NIR}, μ and N is explored. Deposition temperature, H_2O partial pressure and thickness are set at 25 °C, $3.0\cdot10^{-5}$ mbar and 190 nm respectively. Subsequently, the deposited samples undergo annealing in ambient conditions at temperatures of 130, 180, 200, and 250 °C for 20 min.

Fig. 2 shows how increasing the annealing temperature (T_a) decreases N and therefore α_{NIR} values, while simultaneously enhancing μ. A plateau occurs at 200 °C, representing the optimized PDA temperature for IOH, in line with other studies on the impact of PDA treatment on the optoelectrical properties of IOH [32,33]. The power density is chosen to be 1.5 W/cm^{2} on account of the best optoelectrical outcome seen in Fig. 2.

To gain a more comprehensive insight into the improvement of optoelectrical properties in IOH, the XRD characterization is conducted on a sample deposited under optimized deposition parameters before and after the annealing process.

In Fig. 3, the IOH sample appears in an amorphous phase in its as-deposited condition. After ambient PDA, the film exhibits prominent XRD peaks at 2θ = 24.9°, 35.6°, 41.4°, and 59.9°, corresponding to the (211), (222), (400), and (440) planes of polycrystalline In_2O_3 with a cubic bixbyite structure. Particularly, the dominance of the peak at 35.6° indicates that there is a preference for the (222) orientation, which is consistent with previous findings [32,34].

The enhanced optoelectrical properties of IOH films can accordingly be attributed to a phase shift in the atomic structure, transitioning from an amorphous phase to a polycrystalline phase.

Additionally, various annealing techniques are examined to optimize the optical transparency of IOH mono-film on glass, with the sample thicknesses detailed in Table 2. Each annealing process is conducted for 20 min at a temperature of 200 °C on IOH samples deposited using the optimized power density at room temperature, with a H_2O p.p. of $3.0\cdot10^{-5}$ mbar.

As illustrated in Fig. 4, the ambient and vacuum annealing techniques yield consistent results and prove to be the most effective methods for enhancing T in the NIR region.

Table 2 shows the electrical properties of IOH samples in as-deposited condition and under PDA treatments. Both ambient and vacuum annealing exhibit the most significant improvements in electrical properties, highlighting that vacuum annealing achieves the highest mobility (67.28 cm^{2}/Vs), while ambient annealing results in the lowest carrier concentration ($1.94\cdot10^{20}$ cm^{-3}). Overall, ambient annealing achieves the most balanced improvement in optoelectrical properties, effectively enhancing both transparency and electrical conductivity.

As detailed in the study by C. Han et al. [35], these improvements can be attributed to the reduction in Urbach energy (E_U), which indicates the width of the tail of localized defect states in the band gap in low-crystalline, disordered or amorphous materials [36]. Lower E_U values lead to enhanced transparency and reduced reflectance, as well as better electrical properties due to decreased charge carrier scattering and fewer charge traps. Conversely, H_2 annealing might results in higher

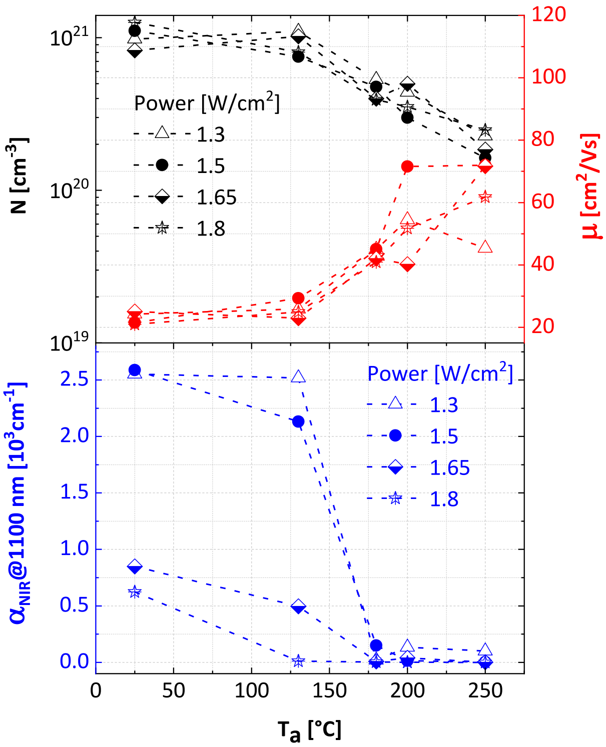

Fig. 2. Processed IOH samples at different power densities [W/cm^{2}]: mobility [cm^{2}/Vs] and carrier concentration [cm^{-3}] vs annealing temperature [°C] (plot above); absorption coefficient [cm^{-1}] @ λ = 1100 nm vs annealing temperature [°C] (plot below).

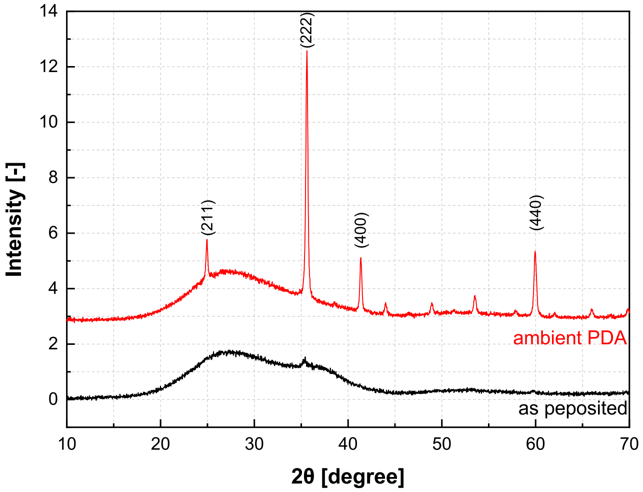

Fig. 3. XRD results for the IOH sample under optimized sputtering parameters, in the as-deposited state, and after 20 min ambient PDA at 200 °C.

Table 2
Hall mobility [cm^2/Vs], carrier concentration [cm^{-3}], sheet resistance [Ω/sq], mini-RT thickness [nm] for IOH films in as deposited condition and under different annealing treatments at 200 °C for 20 min.

sample	μ [cm^2/Vs]	N [10^{20} cm^{-3}]	R_{sh} [Ω/sq]	t [nm]
as-dep.	26.13	5.17	35.81	128.80
ambient an.	66.65	1.94	26.66	140.00
vacuum an.	67.28	2.92	20.15	139.90
H_2-an.	47.09	3.54	27.22	119.80

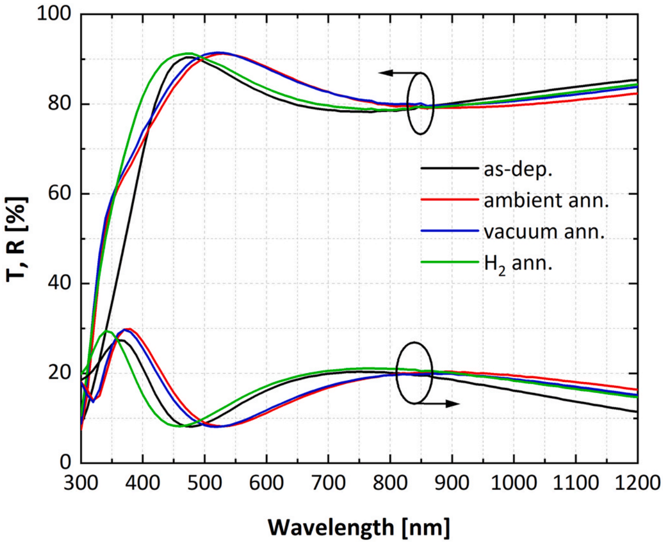

Fig. 4. Reflectance [%] and transmittance [%] of IOH sample as deposited and after ambient, vacuum and H_2 annealing treatments.

E_U values, implying increased band tail states and promoted atomic structural disorder, thus resulting in less improved material quality during the annealing process [37].

3.3. Intrinsic zinc oxide deposition parameters optimization

As illustrated in Fig. 3, the intrinsic zinc oxide samples exhibit the lowest parasitic absorption in the near-infrared region of the solar spectrum, but they are highly resistive TCOs. Therefore, the optimization of the ZnO monolayers is primarily focused on the optical function within the bilayer structure. Unlike the approach taken with IOH, the PDA treatment on ZnO does not induce significant changes in its polycrystalline nature or optoelectrical properties, making it not worth reporting.

Instead, Fig. 5 presents the refractive index (n) and extinction coefficient (k) behaviors of ZnO mono-film samples deposited on glass at different power densities [2.0 3.0 4.0 W/cm^2] at a set substrate temperature of 95 °C. It is worth noting that depositing ZnO at temperatures higher than the optimized IOH annealing temperature (T_a) could inadvertently affect the IOH optoelectrical properties, considering the application of ZnO on top of IOH in a bilayer configuration.

The sample deposited at 2.0 W/cm^2 displays the widest transparency window, as indicated by the extinction coefficient trend, and an increased energy bandgap ($E_g = 3.07$ eV). Lower deposition power enables more controlled and gradual growth of ZnO films, reducing the likelihood of defects such as vacancies and interstitials that scatter light. With fewer defects and impurities, the ZnO film exhibits higher optical transparency [38,39]. Additionally, higher power results in increased energy associated with ion bombardment, which can detrimentally affect the surface morphology of ZnO and the underlying IOH layer [40].

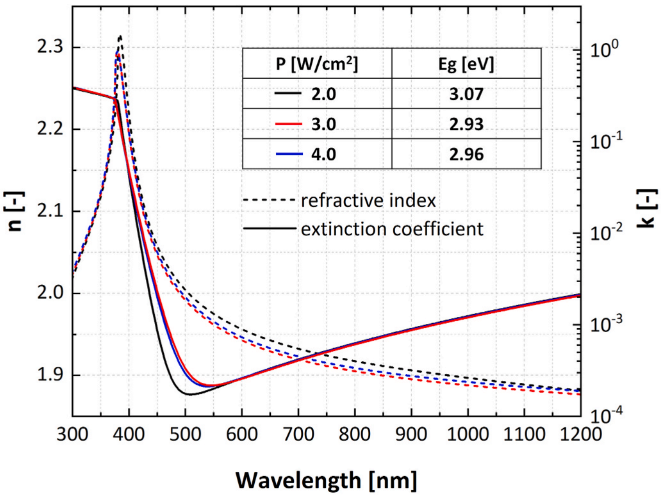

Fig. 5. Refractive index and extinction coefficient behaviors of ZnO samples by varying power density at a constant substrate temperature of 95 °C. Energy bandgap [eV] of sputtered films is mentioned in the table.

3.4. Bilayer optimization based on system geometry assessment

After optimizing the individual properties of both the IOH and ZnO layers, these materials are combined into a bilayer structure to serve as the front contact in solar cells. This combination takes advantage of the high transparency and optimized electrical properties of each layer. Specifically, the bilayer is developed by first depositing the IOH layer on glass for its excellent lateral conductivity, followed by the deposition of the ZnO layer on top to provide superior transparency and transverse conductivity.

To enhance the bilayer design, a series of annealing time is conducted on three samples. The PDA treatment is performed in ambient atmosphere at a fixed temperature of 200 °C, after the complete deposition of both the IOH and ZnO layers. This process follows the previously optimized sputtering parameters for the IOH and ZnO layers.

The thicknesses of the IOH and ZnO layers for each bilayer are summarized in Table 3. Different ZnO thicknesses are chosen to investigate the potential influence of the formation of columnar ZnO crystallites and their subsequent impact on optoelectrical properties.

In this experiment, the most relevant optoelectrical metrics under consideration are the absorptance, the mobility and the carrier concentration.

Fig. 6 illustrates how the gradual increase in annealing time results in stabilized values for both μ and N. In Bilayer III, the mobility is at its peak with a value of 120 cm^2/Vs, and the respective carrier density is $1.97 \cdot 10^{19}$ cm^{-3}. It is worth noting that, in the as-deposited condition, the free carrier density is predominantly influenced by the ZnO layer. However, after the PDA treatment, the N of the bilayer structure reflects a combined contribution from both the ZnO and IOH layers.

Furthermore, the absorptance profile of Bilayer III is examined in its as-deposited condition and after 2 h and 30 min of ambient annealing at 200 °C. Fig. 7 demonstrates the positive influence of PDA on the reduction of parasitic absorptions in both the band-to-band and the NIR regions of the solar spectrum. Wavelengths above 1000 nm show a visible FCA reduction after the PDA treatment in agreement with the

Table 3
IOH and ZnO layer thicknesses [nm] in bilayer structures for the PDA time optimization.

Bilayer ID	IOH thickness [nm]	ZnO thickness [nm]
I	113	655
II	113	587
III	113	519

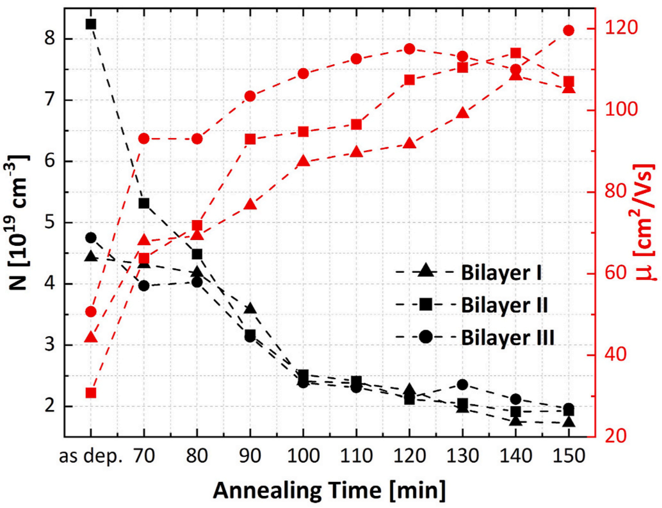

Fig. 6. Carrier concentration [cm^{-3}] and mobility [cm^2/Vs] of bilayers as a function of annealing time [min]. PDA is performed in ambient at 200 °C.

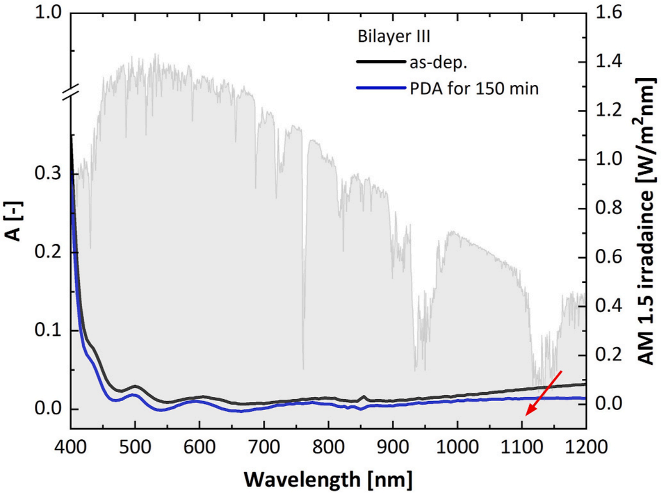

Fig. 7. Absorptance [−] as a function of wavelength [nm] for Bilayer III: black trend represents as deposited condition, blue profile shows 150 min of ambient annealing at 200 °C.

carrier density trend from Fig. 6.

The absorptance characteristics of Bilayer III are analyzed in its initial deposited state and following 2 h and 30 min of ambient annealing at 200 °C. Fig. 7 illustrates the beneficial impact of PDA on decreasing parasitic absorptions across both the band-to-band and in the NIR region of the solar spectrum. Wavelengths beyond 1000 nm exhibit noticeable reductions in FCA after PDA treatment, consistent with the carrier density trends observed in Fig. 6.

Besides the excellent optical improvements and the high mobility being achieved with an annealing time of 150 min, the optimized time for annealed bilayer samples is selected to be 140 min. This choice is grounded in the unvarying findings from multiple experiments, demonstrating that the best optoelectrical trade-off is consistently observed after 2 h and 20 min of PDA treatment.

3.4.1. *Material properties: SEM, AFM, XRD characterization*

Scanning electron microscopy (SEM) and atomic force microscopy (AFM) are employed as techniques for the material characterization of bilayer structure. They provide insights into the surface characteristics and aid the optimization of bilayers fabrication process.

The SEM cross section and top view imagines are taken to investigate the structural growth of bilayer. IOH exhibits a uniformly sputtered deposition on flat glass, reaching an approximate thickness of 70 nm, with crystal grains that are significantly smaller compared to those of ZnO. Above the IOH layer, a progressive increase in structural grains is observed with the growth of ZnO thickness, reaching 1.5 μm. This development results in the formation of larger grains on top of smaller ZnO grains (Fig. 8a and b).

Fig. 8c and 8d demonstrate how the development of ZnO grains contributes to a surface with nano-featured characteristics in the bilayer design. In particular, Fig. 8d highlights the presence of filaments within a single ZnO grain, indicating the preferred growth orientation of the material.

Fig. 9 presents both top and three-dimensional (3D) views of two representative bilayer samples. In particular, Fig. 9a and 9b differ with respect to the thickness of ZnO and, the thickness of IOH remains approximately 100 nm for both cases. Fig. 9a features a deposition of 500 nm of ZnO, and Fig. 9b exhibits a thicker layer with 1 μm of ZnO deposited. These images offer a visual representation of the morphological variations. Grains with larger size can be embedded as the thickness of the ZnO layer increases.

Furthermore, X-ray diffraction (XRD) is utilized for probing the crystalline structure and phase composition of the transparent conductive bilayer. In this study, both IOH and ZnO films incorporated within the bilayer design are deposited using the previously optimized parameters. The bilayer is examined under two conditions: as deposited and following 140 min of ambient PDA treatment at 200 °C.

As depicted in Fig. 10, notable alterations are observed in the intensity of the IOH crystalline peaks, indicating a shift from an amorphous to a more crystalline phase. Moreover, a slight enhancement of the dominant orientation (002) of ZnO is apparent, showing a polycrystalline character of this layer regardless annealing. This is often the preferred orientation for ZnO films grown on various substrates, such as glass [41,42].

3.4.2. *Scattering mechanisms on TCOs opto-electrical properties*

Fig. 11 displays the Hall measurements conducted on various as deposited and annealed IOH and ZnO monolayers, as well as on bilayer structures incorporating IOH and ZnO. The Hall mobility and carrier concentration measured in the bilayers represent average values across the combined layers. These metrics are critical for assessing the performance of TCOs as front contacts in solar cells. High mobility ensures efficient lateral transport of charge carriers, reducing resistive losses, while an optimal carrier concentration balances electrical conductivity and optical transparency. The plot also illustrates the relevant scattering mechanisms limiting the Hall mobility at varying carrier concentrations.

The ZnO monolayers are deposited by varying power density and temperature settings ranging from 2.0 to 4.0 W/cm^2 and from 95 to 217 °C respectively. All other sputtering parameters remained constant, consistent with previous sections of this study. The investigation into the influence of deposition P and T on μ and N yields scattered results, and there does not seem to be a clear trend on whereas the annealing improves the performance.

The challenge in probing zinc oxide as an undoped material lies in the difficulty of laterally extracting free carriers from the material. This limitation suggests that low mobility values are predominantly influenced by the presence of grain boundaries.

For Hydrogenated Indium Oxide, values are illustrated based on power density variation while maintaining all other sputtering settings consistent with the analysis detailed above (refer to Fig. 2). It is evident that PDA treatment positively affects both mobility and carrier concentration across all IOH samples. The findings suggest that ionized impurity scattering emerges as the predominant mechanism limiting free carrier transport. Additionally, a high mobility of 71.57 cm^2/Vs is obtained at a carrier concentration of ~ 10^{20} cm^{-3} in IOH.

Bilayer samples are fabricated using the previously optimized

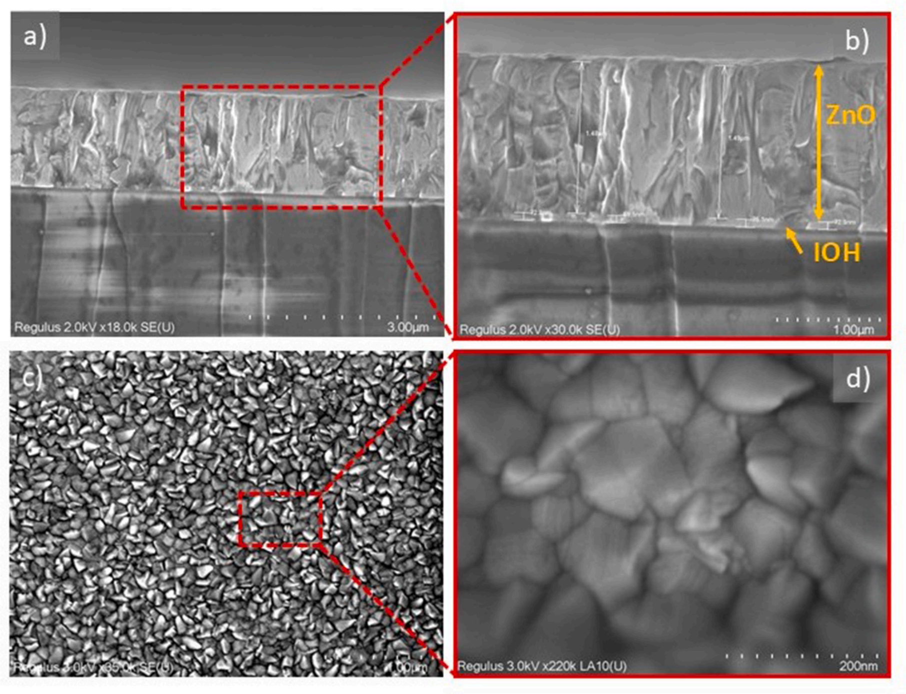

Fig. 8. SEM cross section images (a and b) and top view images (c and d). Cross section images reveal a bilayer with 70 nm IOH and 1.5 μm ZnO. The top view images highlight sharp nano features from ZnO.

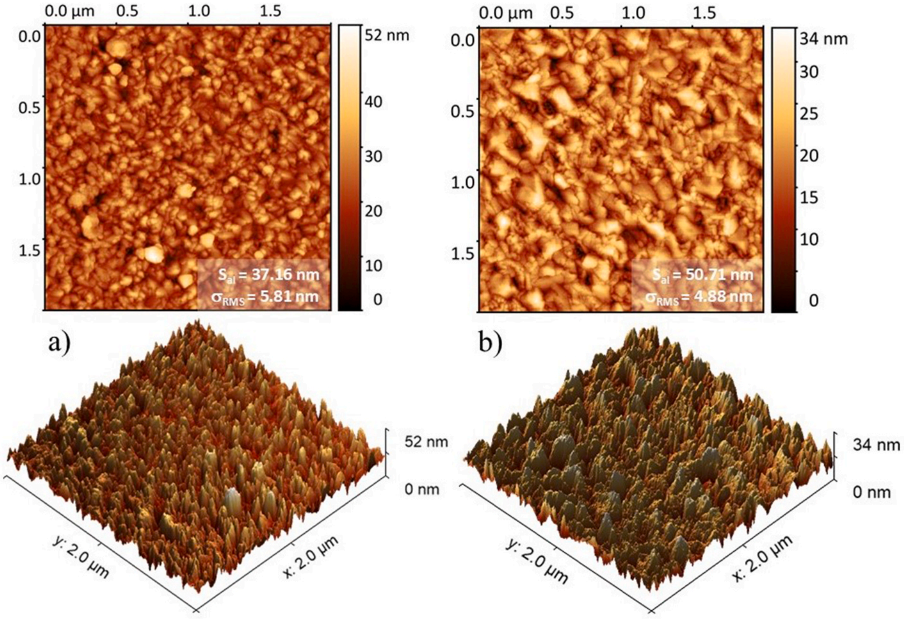

Fig. 9. AFM top and 3D views of bilayers. (a) Bilayer with 100 nm of Hydrogenated Indium Oxide (IOH) and 500 nm of Zinc Oxide (ZnO), while (b) shows a bilayer with 100 nm of IOH and a thicker layer of 1 μm ZnO.

settings. The thickness of IOH is varied, while the desired thickness of ZnO maintained at approximately 600 nm in each bilayer. For each thickness configuration, three samples are fabricated, and their mobility and carrier concentration values are presented in Fig. 11. Table 4 showcases the best outcome in terms of electrical properties for each bilayer thickness configuration following PDA treatment. Additionally, the values of μ and N are also reported in the as-deposited condition to highlight the beneficial impact of ambient annealing on the samples (see Table 4).

Fig. 11 underlines that the mobility of as deposited bilayers is capped by grain boundary scattering and ionized impurity limits ($\mu_{tot}^{-1} = \mu_{GB}^{-1} + \mu_{II}^{-1}$) [44]. In contrast, annealed bilayers exhibit a consistent trend wherein the grain boundary scattering mechanism no longer limits mobility [45–47]. Consequently, the bilayers are nearing the ionized impurity limit, demonstrating higher mobility values at lower carrier concentrations of approximately $\sim 10^{19}$ cm^{-3}.

3.4.3. *Bilayer design geometry interpretation*

This section aims to explain the charge transport mechanism responsible for the enhanced optoelectrical performance observed in the

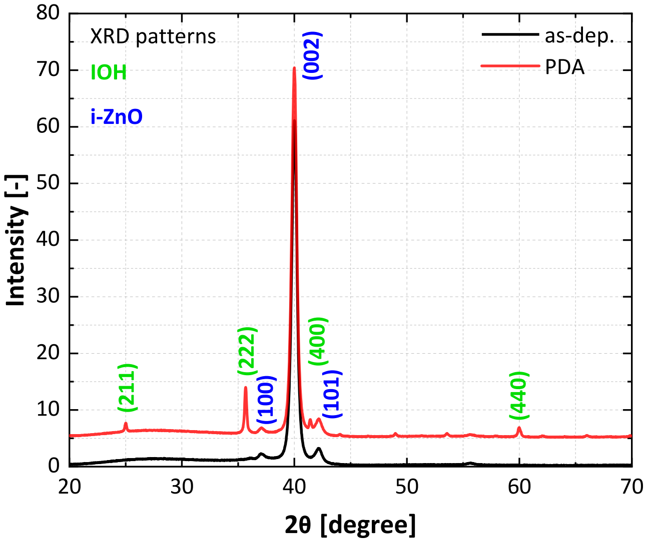

Fig. 10. XRD results for the bilayer sample under optimized sputtering parameters, both in the as-deposited state and after 2 h 20 min ambient PDA at 200 °C. The crystalline phases of IOH and ZnO within the bilayer structure are highlighted in red and blue respectively. The preferred crystal orientation is indicated as (222) for IOH and (002) for ZnO.

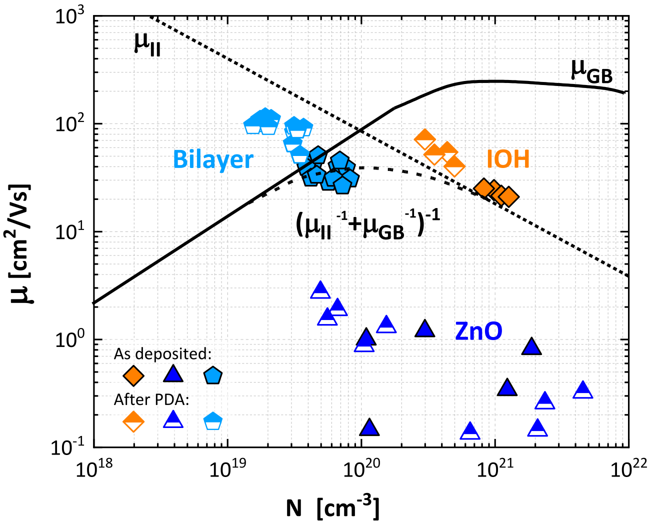

Fig. 11. Measured Hall mobility [cm^2/Vs] versus carrier concentration [cm-3] of undoped ZnO, IOH monolayers and, IOH/ZnO bilayers design. The upper dotted line represents the ionized impurity (II) scattering limit using the Brooks-Herring-Dingle theory and taking into account non-parabolicity of the TCOs conduction band. The full line shows the grain-boundary scattering mechanism for doped and undoped ZnO films. The dashed trend combines grain boundary-limited transport with ionized impurity scattering [24,43].

Table 4
Hall mobility [cm^2/Vs], carrier concentration [cm^{-3}], mini-RT thickness [nm] for bilayers in as deposited condition and after PDA treatment at 200 °C for 2h 20 min.

t_{IOH} [nm] in bilayer	as deposited		PDA	
	μ [cm^2/Vs]	N [10^{19} cm^{-3}]	μ [cm^2/Vs]	N [10^{19} cm^{-3}]
144	39.01	7.71	94.80	3.14
113	30.80	8.24	114.0	1.91
81	39.45	3.88	99.70	1.65
70	33.35	4.64	87.40	3.34

IOH/ZnO bilayer structure. The correlation between IOH crystallization and the enhancement in the optoelectrical properties of bilayers suggests that the post-deposition annealing treatment plays a crucial role in charge transport optimization. As shown in Figs. 10 and 11, the transition from an amorphous to a crystalline phase in IOH, along with improved ZnO orientation, contributes to the observed mobility enhancement.

The mobility of free charge carriers in ZnO is inherently limited by two dominant scattering mechanisms: the ionized impurity scattering (within a single grain) and the grain boundary scattering (in a polycrystalline structure) [48–50].

In a single, sufficiently large ZnO grain, the charge carrier mobility is primarily limited by ionized impurity scattering, which occurs due to Coulombic interactions between free electrons and ionized dopants [51]. This scattering disrupts carrier motion and sets an intrinsic upper bound on mobility. The corresponding limit is described by the Brooks-Herring-Dingle model as depicted in Fig. 11. With increased carrier density, enhanced Coulombic scattering reduces the carrier mean free path, thereby decreasing mobility [24].

In a polycrystalline ZnO film, the mobility is further restricted by grain boundary scattering, where the charge carriers encounter potential barriers at grain interfaces due to trapped charge states. The models of Seto and Baccarani et al. yield an effective mobility μ_{eff} dominated by thermionic emission across the grain barriers [52]:

$$\mu_{eff} = \mu_0 \exp(-\Phi_b / k_B T) \tag{3.1}$$

The energetic barrier height is Φ_b at the grain boundary, T is the sample temperature, and k_B is the Boltzmann constant. The prefactor μ_0 represents the mobility inside a grain [53,54].

The presence of grain boundaries therefore forces the free charge carriers to undergo thermionic emission or tunneling, significantly restricting lateral transport. Consequently, the charge transport in ZnO-dominated bilayers is largely transverse, as lateral mobility is constrained by grain boundary effects.

As revealed in Fig. 11, the Hall mobility in the bilayer structure is significantly higher than that of a single-layer IOH. It suggests that lateral conduction occurs preferentially at the IOH/ZnO interface rather than within the bulk IOH layer. This effect is directly correlated with the PDA treatment, which facilitates the crystallization of IOH, leading to the formation of a more conductive interfacial pathway.

The band alignment between IOH and ZnO may induce charge redistribution, forming an accumulation layer at the interface. This generates an internal electric field that enhances lateral carrier transport, reducing scattering and improving mobility [55,56]. The effect follows a parallel transport model where the interface conductivity ($\sigma_{interface}$) significantly contributes to the bilayer overall conductivity ($\sigma_{bilayer} = \sigma_{IOH} + \sigma_{interface}$) [57].

It implies that free carrier lateral transport occurs within a certain penetration depth in the IOH material, defined as the portion of the IOH thickness near the interface with ZnO that allows free charge carriers to circumvent the ZnO grains. The interpretation of the free charge carrier transport in the bilayer geometry is visually explained in Fig. 12 through a simplified sketch.

An IOH thickness of 70 nm may not be adequate to bypass the grains, as demonstrated by the properties in Table 5. Conversely, thicker IOH material may lead to a situation where the transport of some carriers occurs within the bulk of the IOH material rather than exclusively at the interface, resulting in a decrease in mobility and an increase in carrier density. This leads to the conclusion that bypassing free carrier transport is favorable when the thickness of the conductive layer in the bilayer structure falls within the range of the penetration depth of free electrons, which is approximately between 80 and 110 nm.

Furthermore, the 'effective' carrier density value for the bilayer ($N_{bilayer}$), measured using the Hall effect setup, can be approximated as:

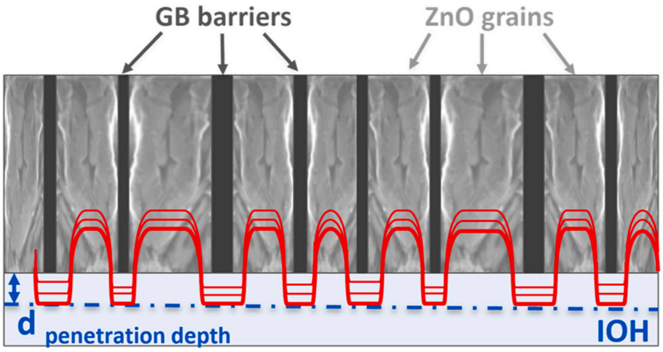

Fig. 12. Simplified sketch illustrating the bilayer geometry and the role of the interface between IOH and ZnO layers in facilitating free carrier transport. Undoped zinc oxide grains and grain boundary (GB) barriers are depicted in light and dark grey respectively. Free charge carrier transport bypassing the grain boundaries is shown in red, while the penetration depth of this transport mechanism within the IOH layer is highlighted in blue.

$$N_{\text{bilayer}} \approx \frac{d_{\text{IOH,pen.depth}}}{d_{\text{IOH,pen.depth}} + d_{\text{ZnO}}} \cdot N_{\text{IOH}} \tag{3.2}$$

In Formula 3.2, $d_{\text{IOH,pen.depth}}$ refers to the portion of the IOH thickness near the interface with ZnO through which free charge carriers bypass the ZnO grains, d_{ZnO} is the thickness of ZnO layer, and N_{IOH} is the carrier density in the IOH layer. Notably, the experimental findings in Fig. 11 align well with the theoretical prediction. The Hall carrier concentration in the bilayer is reduced by approximately one order of magnitude ($\sim 10^{19}$ cm^{-3}) compared to the single-layer IOH structure. This agreement further reinforces the validity of the proposed transport mechanism and the role of interface-driven charge conduction in the bilayer system.

3.5. *Bilayer design as front contact in nc-Si:H single junction solar cell for R_s measurements*

To test both the optical and electrical properties of the bilayer concept, it is integrated as the front contact in nc-Si:H solar cells. For comparison, identical solar cells are processed with single-layer ITO or IOH as the front contact. It is important to note that while the performance of these solar cells demonstrates the impact of the front contact layers, it does not reach record levels.

Fig. 13 presents the JV characteristics of 0.16 cm^2 nc-Si:H solar cells, comparing the three different front contact designs under investigation. Additionally, the figure includes a schematic illustration of the solar cell structure for reference. The corresponding measured electrical parameters are summarized in Table 3. For further details regarding the solar cell fabrication process and structural configuration, refer to Section 2.4.

The IOH front contact provides a slight improvement in the V_{oc} value and a notable increase in the J_{sc} value compared to the ITO front contact, leading to a higher fill factor and efficiency. This can be attributed to the enhanced optoelectrical properties of the optimized IOH layer, as described in Section 3.2, which improves charge carrier collection and reduces recombination losses.

For the ITO monolayer, the material is selected based on the best optoelectrical trade-off observed in Fig. 1, where the absorption coefficient versus resistivity of ITO is studied. This optimized ITO is then used as the front contact for a fair comparison with the IOH and bilayer structures.

The improved fill factor and overall efficiency of the cell with the bilayer are linked to a reduction in series resistance and a slight increase in shunt resistance. The IOH and ZnO bilayer appears to lower series resistance in solar cells by combining the high conductivity and excellent interface properties of both materials. The bilayer structure, being

Table 5
External electrical parameters of the best nc-Si:H solar cell for each front contact configuration (ITO, IOH, and IOH/ZnO bilayer). The reported short circuit current density [mA/cm^2] is based on the EQE measurements. The series resistance (R_s) and the shunt resistance (R_{sh}) values are also provided for each configuration.

TCO	V_{oc} [V]	$J_{sc,EQE}$ [mA/ cm^2]	FF [%]	η [%]	R_s [Ω cm^2]	R_{sh} [Ω cm^2]
ITO	0.52	23.56	56.27	6.89	23.99	1965 0.16
IOH	0.53	25.22	58.25	7.79	23.65	2051.28
bilayer	0.51	23.85	64.56	7.85	9.81	2481.95

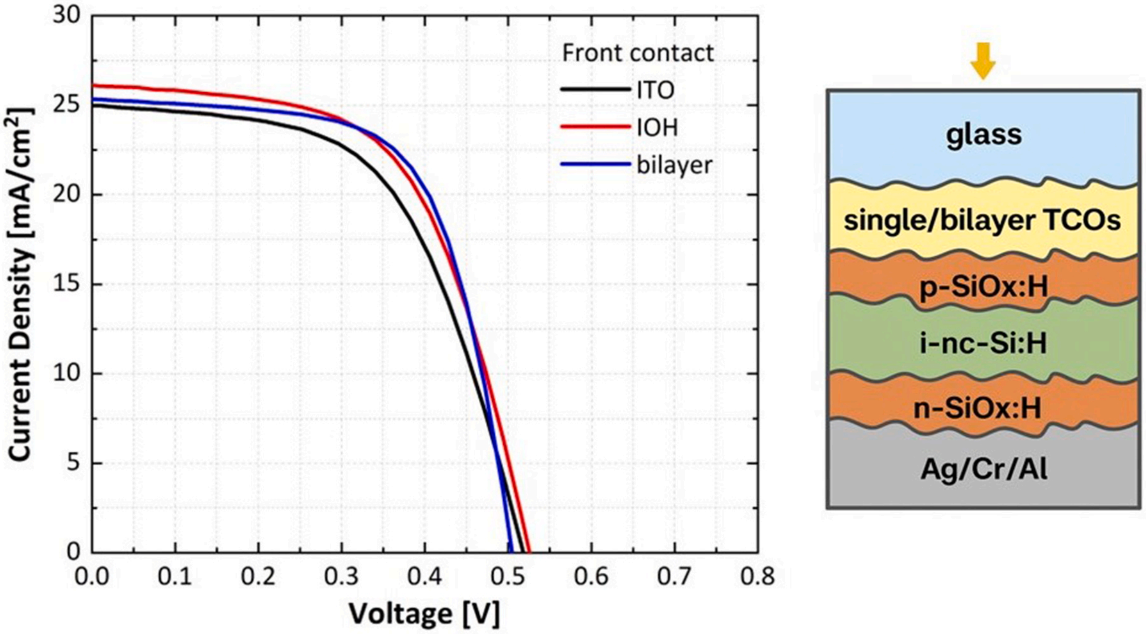

Fig. 13. Current-voltage characteristics of the best nc-Si:H solar cell for each front contact configuration (ITO, IOH, and IOH/ZnO bilayer), along with a cross-sectional schematic of the p-i-n structure (layer thicknesses not to scale).

thicker than the IOH or ITO single-layer front contacts, introduces an interplay between its optimized optoelectrical properties and thickness. Consequently, the thicker bilayer configuration is expected to contribute to a reduction in series resistance. This demonstrates that a bilayer configuration can decouple the optical and electrical properties of a TCO front contact while preserving or even improving the performance of a solar cell.

Fig. 14 shows the external quantum efficiency and reflection loss profiles of the best-performing solar cells with different front contact configurations. The EQE plot for the bilayer structure reveals a significant reduction at shorter wavelengths, indicating that the lower EQE arises from the decreased absorption in the nc-Si:H absorber layer. This reduction is attributed to increased parasitic absorption in the ZnO layer, which has a lower energy bandgap compared to IOH and ITO. Hence, the EQE-derived current density is higher in the solar cell with IOH as front contact than in the one with the IOH/ZnO bilayer structure.

Furthermore, the EQE profiles of solar cells with IOH and the bilayer are comparable in the NIR region, with both outperforming the ITO configuration. Despite the high energy bandgap of ITO, its performance in the NIR region is limited by significantly higher free carrier absorption.

The reflection losses, as observed in the 1-R curves, reveal distinct interference patterns for the various front contact configurations. The blue trend, corresponding to the solar cell with the thick bilayer as the front contact, exhibits clear interference effects across the wavelength range due to its increased thickness. In contrast, the red and black trends, representing the thinner IOH and ITO front contacts, show pronounced interference primarily at shorter wavelengths. Notably, the IOH fringe limits the blue response of the IOH-based cell. Optimizing the interaction between the TCO layers and the textured substrate could further reduce these optical interference effects.

4. Conclusion

This study demonstrates the significant advancements achieved by employing a bilayer front contact design in thin-film solar cells, specifically utilizing hydrogenated indium oxide (IOH) and non-intentionally doped zinc oxide (ZnO). Through meticulous optimization of deposition parameters and post-deposition annealing (PDA) conditions, this research effectively enhances the optoelectrical performance of transparent conductive oxides (TCOs).

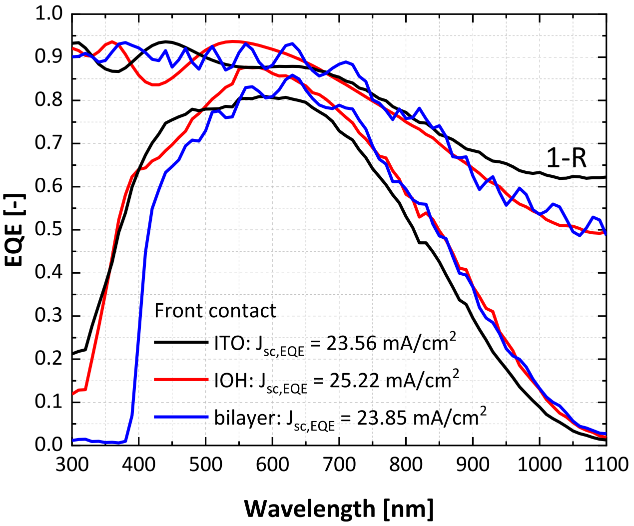

Fig. 14. External quantum efficiency (EQE) curves of the best nc-Si:H solar cell for each front contact configuration (ITO, IOH, and IOH/ZnO bilayer). The plot also includes the 1-R curves, representing the front reflection losses.

The resulting bilayer structure, featuring IOH for its exceptional conductivity and ZnO for its minimal parasitic absorption in the near-infrared region, delivers superior optoelectrical properties, achieving a mobility of 120 cm^2/Vs and a carrier density of 1.97 × 10^{19} cm^{-3}. Incorporating this bilayer structure as the front electrode in hydrogenated nanocrystalline silicon (nc-Si:H) solar cells demonstrates its practical effectiveness.

The differences compared to other front contact designs are relatively modest, and no record-breaking efficiencies are achieved. However, the true value of the bilayer approach lies in the enhanced design flexibility it offers. Rather than relying on a single TCO to simultaneously balance high conductivity and optical transparency, the bilayer configuration enables the decoupling of these optoelectrical properties between two TCO layers. Each TCO is optimized for a specific function: one for high conductivity (e.g., IOH) and one for minimal free carrier absorption (e.g., ZnO).

Moreover, the interaction at the interface between the two layers offers distinct advantages for optimizing solar cell performance beyond what could be achieved by simply averaging the properties of the individual layers. Notable effects, such as improved lateral carrier transport and reduced recombination at the interface, can significantly contribute to the overall performance.

Future work should focus on optimizing the thickness of the conductive and transparent layers in the bilayer structure, as well as carefully controlling the annealing process to enhance crystallization. These refinements could further improve optoelectrical performance and lead to greater efficiency gains. Additionally, exploring indium-free TCO alternatives for the bilayer concept offers a promising path to reduce reliance on the scarce indium material. Using more abundant materials could enhance the scalability of the bilayer approach in solar cell technologies.

To conclude, the bilayer approach opens new possibilities for designing TCOs in thin-film solar cells, providing a flexible and potentially more effective pathway to improving the performance of solar cell technologies.

CRediT authorship contribution statement

Federica Saitta: Writing – review & editing, Writing – original draft, Visualization, Supervision, Methodology, Investigation, Formal analysis, Data curation, Conceptualization. **Prashand Kalpoe:** Methodology, Investigation, Data curation. **Vidur Ahluwalia:** Methodology, Investigation, Data curation. **Govind Padmakumar:** Writing – review & editing, Methodology, Investigation, Formal analysis, Data curation, Conceptualization. **Paula Perez Rodriguez:** Writing – review & editing, Visualization, Supervision, Methodology, Investigation, Formal analysis. **Gianluca Limodio:** Writing – review & editing, Visualization, Supervision, Methodology, Formal analysis, Data curation, Conceptualization. **Rudi Santbergen:** Writing – review & editing, Supervision, Methodology, Formal analysis, Data curation, Conceptualization. **Arno H.M. Smets:** Writing – review & editing, Supervision, Project administration, Methodology, Investigation, Funding acquisition, Formal analysis, Conceptualization.

Declaration of generative AI and AI-assisted technologies in the writing process

During the preparation of this work the main author used ChatGPT in the writing process to improve the readability and the language of the manuscript. After using this service, the authors reviewed and edited the content as needed and take full responsibility for the content of the published article.

Declaration of competing interest

The authors declare the following financial interests/personal relationships which may be considered as potential competing interests: Federica Saitta reports financial support was provided by HyET Solar. If there are other authors, they declare that they have no known competing financial interests or personal relationships that could have appeared to influence the work reported in this paper.

Acknowledgment

The contributions of the students and staff members belonging to the Photovoltaic Materials and Devices (PVMD) group of the Electrical Sustainable Energy department of the Delft University of Technology are gratefully acknowledged. Dhr. Ruud Hendrikx at the Department of Materials Science and Engineering of the Delft University of Technology is acknowledged for the X-ray analysis. Appreciation is also extended to the bilateral collaboration between the HyET Solar company and the Delft University of Technology, which provided essential funding and support for this research.

Data availability

Data will be made available on request.

References

[1] Ganesh T. Chavan, et al., A brief review of transparent conducting oxides (TCO): the influence of different deposition techniques on the efficiency of solar cells, Nanomaterials 13 (7) (2023) 1226.

[2] Małgorzata Musztyfaga-Staszuk, Artur Czupryński, Rossen Radev, Review of the chosen methods of producing front contacts to transparent conductive oxides layers in photovoltaic structures, Energies 15 (23) (2022) 9026.

[3] Christelle Habis, Jean Zaraket, Michel Aillerie, Transparent conductive oxides. Part II. Specific focus on ITO, ZnO-AZO, SnO2-FTO families for photovoltaics applications, in: Defect and Diffusion Forum, 417, Trans Tech Publications Ltd, 2022.

[4] Ayşe Seyhan, Emre Kartal, Optical, electrical and structural properties of ITO/IZO and IZO/ITO multilayer transparent conductive oxide films deposited via radiofrequency magnetron sputtering, Coatings 13 (10) (2023) 1719.

[5] Xinge Yu, J. Tobin, Marks, and antonio facchetti. "Metal oxides for optoelectronic applications", Nat. Mater. 15 (4) (2016) 383–396.

[6] Jessica Patel, et al., A review of transparent conducting films (TCFs): prospective ITO and AZO deposition methods and applications, Nanomaterials 14 (24) (2024) 2013.

[7] K.L. Chopra, S. Major, D.K. Pandya, Transparent conductors—a status review, Thin Solid Films 102 (1) (1983) 1–46.

[8] Hadj Tahar Bel, Radhouane, et al., Tin doped indium oxide thin films: electrical properties, J. Appl. Phys. 83 (5) (1998) 2631–2645.

[9] K. Tamizh Selvi, Suresh Sagadevan, Recent developments in optoelectronic and photonic applications of metal oxides, Metal Oxides for Optoelectronics and Optics-Based Medical Applications (2022) 33–57.

[10] Natalie Preissler, et al., Electrical transport, electrothermal transport, and effective electron mass in single-crystalline in 2 O 3 films, Phys. Rev. B 88 (8) (2013) 085305.

[11] Herman Heffner, Marcos Soldera, Andrés Fabián Lasagni, Optoelectronic performance of indium tin oxide thin films structured by sub-picosecond direct laser interference patterning, Sci. Rep. 13 (1) (2023) 9798.

[12] He Wen, et al., Advancements in transparent conductive oxides for photoelectrochemical applications, Nanomaterials 14 (7) (2024) 591.

[13] Alexander Korneluk, Julia Szymczak, Tomasz Stefaniuk, Annealing-free fabrication of high-quality indium tin oxide films for free-carrier-based hybrid metal–semiconductor nanophotonics, Sci. Rep. 13 (1) (2023) 18520.

[14] Seyed Mohammad Rozati, Seyed Ashkan Moghadam Ziabari, A review of various single layer, bilayer, and multilayer TCO materials and their applications, Mater. Chem. Phys. 292 (2022) 126789.

[15] Yih-Shing Lee, et al., Investigation into the characteristics of double-layer transparent conductive oxide ITO/TNO anti-reflection coating for silicon solar cells, Crystals 13 (1) (2023) 80.

[16] Xia Yan, et al., Surface texturing studies of bilayer transparent conductive oxide (TCO) structures as front electrode for thin-film silicon solar cells, J. Mater. Sci. Mater. Electron. 26 (2015) 7049–7058.

[17] Dibyendu Kumar Ghosh, et al., Realization of performance enhancement of thin film silicon solar cells by applying ITO/AZO bilayer TCO films as front electrode, J. Mater. Sci. Mater. Electron. 34 (33) (2023) 2189.

[18] Mahdiyar Nouri Rezaie, et al., Comparison study of transparent RF-sputtered ITO/AZO and ITO/ZnO bilayers for near UV-OLED applications, Appl. Surf. Sci. 392 (2017) 549–556.

[19] Hairen Tan, et al., Highly transparent modulated surface textured front electrodes for high-efficiency multijunction thin-film silicon solar cells, Prog. Photovoltaics Res. Appl. 23 (8) (2015) 949–963.

[20] Zhongming Du, et al., Robust AZO/i-ZnO bilayer front contact for high-performance thin film solar cells, RSC Adv. 6.109 (2016) 108067–108074.

[21] Huiyong Liu, et al., Transparent conducting oxides for electrode applications in light emitting and absorbing devices, Superlattice. Microst. 48 (5) (2010) 458–484.

[22] Corsin Battaglia, et al., Micromorph thin-film silicon solar cells with transparent high-mobility hydrogenated indium oxide front electrodes, J. Appl. Phys. 109 (2011) 11.

[23] L. Barraud, et al., Hydrogen-doped indium oxide/indium tin oxide bilayers for high-efficiency silicon heterojunction solar cells, Sol. Energy Mater. Sol. Cell. 115 (2013) 151–156.

[24] Tadatsugu Minami, New n-type transparent conducting oxides, MRS Bull. 25 (8) (2000) 38–44.

[25] K.G. Saw, et al., New insights on the burstein-moss shift and band gap narrowing in indium-doped zinc oxide thin films, PLoS One 10 (10) (2015) e0141180.

[26] Zhewei Wang, et al., Transparent conductive oxides and their applications in near infrared plasmonics, Phys. Status Solidi 216 (5) (2019) 1700794 f.

[27] Harm Knoops, et al., Optical modeling of plasma-deposited ZnO films: electron scattering at different length scales, J. Vac. Sci. Technol. A 33 (2015) 2.

[28] Julia R. D'Rozario, et al., Modeling free-carrier absorption in ultrathin III-V solar cells with light management, Opt. Express 30 (5) (2022) 7096–7109.

[29] Hairen Tan, et al., Micro-textures for efficient light trapping and improved electrical performance in thin-film nanocrystalline silicon solar cells, Appl. Phys. Lett. 103 (2013) 17.

[30] Mathieu Boccard, Nathan Rodkey, Zachary C. Holman, High-mobility hydrogenated indium oxide without introducing water during sputtering, Energy Proc. 92 (2016) 297–303.

[31] Taiki Kataoka, et al., Nondegenerate polycrystalline hydrogen-doped indium oxide (InO X: H) thin films formed by low-temperature solid-phase crystallization for thin film transistors, Materials 15 (1) (2021) 187.

[32] Liangge Xu, et al., Effect of post-deposition annealing on the structural evolution and optoelectronic properties of In2O3: H thin films, Nanomaterials 12 (19) (2022) 3533.

[33] Yusaku Magari, et al., High-mobility hydrogenated polycrystalline In2O3 (In2O3: H) thin-film transistors, Nat. Commun. 13 (1) (2022) 1078.

[34] Darja Erfurt, et al., Improved electrical properties of pulsed DC magnetron sputtered hydrogen doped indium oxide after annealing in air, Mater. Sci. Semicond. Process. 89 (2019) 170–175.

[35] Can Han, et al., Realizing the potential of RF-sputtered hydrogenated fluorine-doped indium oxide as an electrode material for ultrathin SiO x/poly-Si passivating contacts, ACS Appl. Energy Mater. 3 (9) (2020) 8606–8618.

[36] Ahmed Saeed Hassanien, A. Akl Alaa, Effect of Se addition on optical and electrical properties of chalcogenide CdSSe thin films, Superlattice. Microst. 89 (2016) 153–169.

[37] Syeda Arooj, et al., Green emission of indium oxide via hydrogen treatment, RSC Adv. 8 (21) (2018) 11828–11833.

[38] G. Anil Kumar, MV Ramana Reddy, Katta Narasimha Reddy, Structural and Optical properties of ZnO thin films grown on various substrates by RF magnetron sputtering, in: IOP Conference Series: Materials Science and Engineering, vol. 73, IOP Publishing, 2015, p. 1.

[39] A. Ismail, M.J. Abdullah, The structural and optical properties of ZnO thin films prepared at different RF sputtering power, J. King Saud Univ. Sci. 25 (3) (2013) 209–215.

[40] R. Krishna, et al., Nanostructure formation on zinc oxide film by ion bombardment, Nucl. Instrum. Methods Phys. Res. Sect. B Beam Interact. Mater. Atoms 244 (1) (2006) 78–80.

[41] Huawa Yu, et al., ZnO thin films produced by the RF magnetron sputtering, in: Proceedings of 2011 International Conference on Electronic & Mechanical Engineering and Information Technology, vol. 5, IEEE, 2011.

[42] MR Alfaro Cruz, et al., ZnO thin films deposited by RF magnetron sputtering: effects of the annealing and atmosphere conditions on the photocatalytic hydrogen production, Int. J. Hydrogen Energy 43 (22) (2018) 10301–10310.

[43] Yan Ye, Zinc-oxynitride TFTs: toward a new high-mobility low-cost thin-film semiconductor, Inf. Disp. 29 (2) (2013) 20–24.

[44] T. Pisarkiewicz, K. Zakrzewska, E. Leja, Scattering of charge carriers in transparent and conducting thin oxide films with a non-parabolic conduction band, Thin Solid Films 174 (1989) 217–223.

[45] D.H. Zhang, H.L. Ma, Scattering mechanisms of charge carriers in transparent conducting oxide films, Appl. Phys. A 62 (1996) 487–492.

[46] Rakesh A. Afre, et al., Transparent conducting oxide films for various applications: a review, Rev. Adv. Mater. Sci. 53 (1) (2018) 79–89.

[47] Getnet Kacha Deyu, et al., Electrical properties of low-temperature processed Sn-doped In2O3 thin films: the role of microstructure and oxygen content and the potential of defect modulation doping, Materials 12 (14) (2019) 2232.

[48] Klaus Ellmer, Resistivity of polycrystalline zinc oxide films: current status and physical limit, J. Phys. Appl. Phys. 34 (21) (2001) 3097.

[49] M. Chen, et al., Intrinsic limit of electrical properties of transparent conductive oxide films, J. Phys. Appl. Phys. 33 (20) (2000) 2538.

[50] Tadatsugu Minami, Toshihiro Miyata, Hiroki Tokunaga, Electron scattering from disordered grain boundaries in degenerate polycrystalline Al-doped ZnO thin films, Phys. Status Solidi 216 (5) (2019) 1700783.

[51] Klaus Ellmer, Rainald Mientus, Carrier transport in polycrystalline ITO and ZnO: Al II: the influence of grain barriers and boundaries, Thin Solid Films 516 (17) (2008) 5829–5835.

[52] Biswajit Mahapatra, Sanjit Sarkar, Understanding of mobility limiting factors in solution grown Al doped ZnO thin film and its low temperature remedy, Heliyon 8 (10) (2022) e10961.
[53] John YW. Seto, The electrical properties of polycrystalline silicon films, J. Appl. Phys. 46 (12) (1975) 5247–5254.
[54] G. Baccarani, B. Ricco, G.J.O.A.P. Spadini, Transport properties of polycrystalline silicon films, J. Appl. Phys. 49 (11) (1978) 5565–5570.
[55] E. Płaczek-Popko, et al., Carrier transport mechanisms in the ZnO based heterojunctions grown by MBE, Opto-Electron. Rev. 25 (3) (2017) 181–187.
[56] Robert M. Hewlett, A. McLachlan Martyn, Surface structure modification of ZnO and the impact on electronic properties, Adv. Mater. 28 (20) (2016) 3893–3921.
[57] San Kang, et al., Characteristics of an oxide/metal/oxide transparent conducting electrode fabricated with an intermediate Cu–Mo metal composite layer for application in efficient CIGS solar cell, RSC Adv. 7 (76) (2017) 48113–48119.